J. Fluid Mech. (1995), *vol.* 286, *pp.* 117–135

Quantitative characteristics of a laminar, unsteady necklace vortex system at a rectangular block–flat plate juncture

By C. V. SEAL, C. R. SMITH, O. AKIN AND D. ROCKWELL

Department of Mechanical Engineering and Mechanics, Lehigh University, Bethlehem, PA 18015, USA

(Received 9 August 1993 and in revised form 28 September 1994)

The unsteady laminar necklace vortex system formed at the junction of a rectangular bluff body and a flat plate was studied experimentally using hydrogen bubble flow visualization and particle image velocimetry (PIV). The vortex system was found to exhibit unsteady behaviour similar to that described by other investigators for cylinder–flat plate junctures, and is characterized by the periodic formation of necklace vortices upstream of the body that subsequently break away and advect towards the block. Detailed analysis of PIV measurements on the plane of symmetry indicates that the dominant mechanism for vorticity balance in the vortex system is the cross-cancellation of the vorticity of the necklace vortex with vorticity of opposite sign generated by interaction of the necklace vortex with the approach surface to the body.

1. Introduction

When a boundary-layer flow (either laminar or turbulent) encounters a bluff body extending from a surface, a complex, three-dimensional flow field develops in the junction region. These flows occur in many practical applications such as wing-body junctions, turbine blade–hub junctions, and cooling flow past computer chips on a circuit board. Flows of this type can often have profound effects on flow-dependent properties in the junction region, such as local heat transfer rates and skin friction.

Owing to the adverse pressure gradient generated by the presence of the bluff body, the approaching boundary-layer fluid will undergo local flow reversal, creating a region of separation upstream of the body. The impinging boundary layer destabilizes, forming spanwise vortex structures fed by advected vorticity generated upstream at the leading edge of the plate. The body also imposes a cross-stream pressure gradient, causing the boundary layer to divert symmetrically around the body, thus introducing a high degree of three-dimensionality. The end result is the organization of the impinging vorticity into a necklace vortex system (figure 1) in the junction region of the bluff body, which appears as one or more horseshoe-shaped vortices oriented such that the legs of the vortices extend downstream to either side of the body, with the apex of the deformed vortex on the symmetry plane.

These types of necklace vortex flows develop in many real systems and can have significant consequences. For example, at the junction of a conning tower and submarine hull, the formation of a necklace vortex system will cause an increase in both local skin friction, drag, and noise. In addition, the legs of the necklace vortices can extend downstream and interfere with propeller or control surface operation (Lugt 1983). In the case of a turbine blade–hub juncture, the recirculation zones can greatly

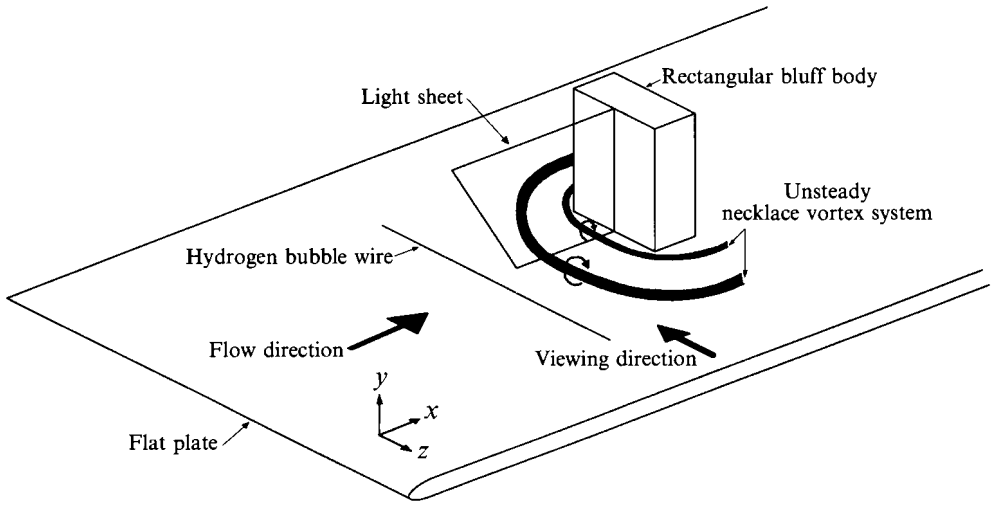

FIGURE 1. Schematic of experimental configuration.

affect local heat transfer rates, increasing thermal gradients in the blade. In addition, increased skin friction owing to necklace vortex development can cause severe erosion at the base of a bridge or pier support.

Necklace vortex systems exhibit a range of steady and unsteady behaviour depending on the Reynolds number (*Re*), boundary-layer thickness, and a characteristic dimension of the body (width, diameter, etc.). Previous studies of unsteady necklace vortex systems include investigations of: the vortex system formed by the interaction of a laminar boundary layer in the junction of a 60° included-angle wedge in air (Schwind 1962); the behaviour at a cylinder–flat plate junction in air with a laminar approach flow (Baker 1979); and the flow behaviour at a cylinder–flat plate juncture for both air and water flows (Thomas 1987). Both Schwind and Baker examined the steady (lower *Re*) as well as periodic unsteady (higher *Re*) necklace vortex regimes, while Thomas concentrated on the unsteady regimes. For a cylinder–flat plate junction with laminar approach flow in water, Greco (1990) provides the most comprehensive classification and description of the range of necklace vortex behaviour. Based on the studies of Greco, the behaviour of a junction necklace vortex system can be generally classified into five regimes:

(i) *Steady*

One, two, or three steady necklace vortices form with the number of vortices increasing as *Re* is increased.

(ii) *Oscillating*

Vortices oscillate periodically with increasing frequency as *Re* increases.

(iii) *Amalgamating*

The primary vortex (the vortex closest to the body) breaks away from the formation region and advects towards the body, but is then drawn back to, and amalgamates with, the secondary vortex (the vortex following the primary vortex), forming a new primary vortex. Amalgamation is a periodic event for which frequency increases as *Re* increases.

(iv) *Breakaway*

The primary vortex periodically breaks away from the formation region and advects downstream towards the body. The frequency of breakaway increases with increasing *Re*.

(v) *Transitional*

The entire system destabilizes into three-dimensional, turbulent-like behaviour.

Little is known of the juncture region of a rectangular bluff body on a flat plate. Norman (1972) investigated the laminar and turbulent vortex system formed in the juncture region of fence-like obstructions using air, and observed basically similar behaviour to that described by Greco. However, Norman did not measure local velocity behaviour or examine the vorticity behaviour involved in these types of flows, nor did he examine wide bodies.

The present study is part of a larger study examining the regimes and frequency behaviour for the necklace vortex system formed at the juncture of a rectangular bluff body with a flat plate, for which the necklace vortex system was shown to progress through essentially the same regimes as those described above for cylinder–flat plate junctures. The present study expands on previous work, which consists mainly of qualitative visualization and limited hot-wire/film measurements, by establishing instantaneous velocity field measurements for a necklace vortex system and employing these measurements to examine the vorticity field/circulation behaviour.

As mentioned above, the necklace vortex system is stimulated by the adverse pressure gradient produced by the presence of the body, which causes (i) flow separation and reversal in the boundary layer near the body, and (ii) subsequent reorganization of advected boundary-layer vorticity into discrete vortices. Since vorticity is continuously generated at the leading edge of the plate, this raises the question of what happens to this vorticity as it approaches the juncture region near the block. If the vorticity were to accumulate continuously in front of the body, the vortex system would grow continuously, which is not the case, since vortex systems of apparently discrete amounts of vorticity exist in one of several modes of either steady or periodic behaviour. Therefore, a vorticity balance must somehow be maintained by the system. Prior computational work by Mason & Morton (1987) has clearly illustrated that surface-mounted obstacles cause the generation of vorticity of opposite sign to the impinging boundary layer vorticity owing to the action of the distributed adverse pressure gradient induced in the approach region to the obstacles. They further illustrate that this generated, opposite-sign vorticity will interact with the original boundary-layer vorticity in a complex process of vorticity cross-cancellation. The present results are complimentary to and extend the work of Mason & Morton, illustrating experimentally how such a process of vorticity generation/cancellation can be both localized and discrete.

The objective of the present study was to examine experimentally how vorticity is distributed within a bluff-body necklace vortex system, and how this vorticity is redistributed to maintain a balance of vorticity. The present study examines a case within the breakaway regime, since this type of regime exhibits both periodic vorticity reorganization, and clear vortex–surface interactions. The study employs both qualitative assessment using hydrogen-bubble flow visualization and quantitative measurement of velocity field behaviour using high image-density particle image velocimetry (PIV).

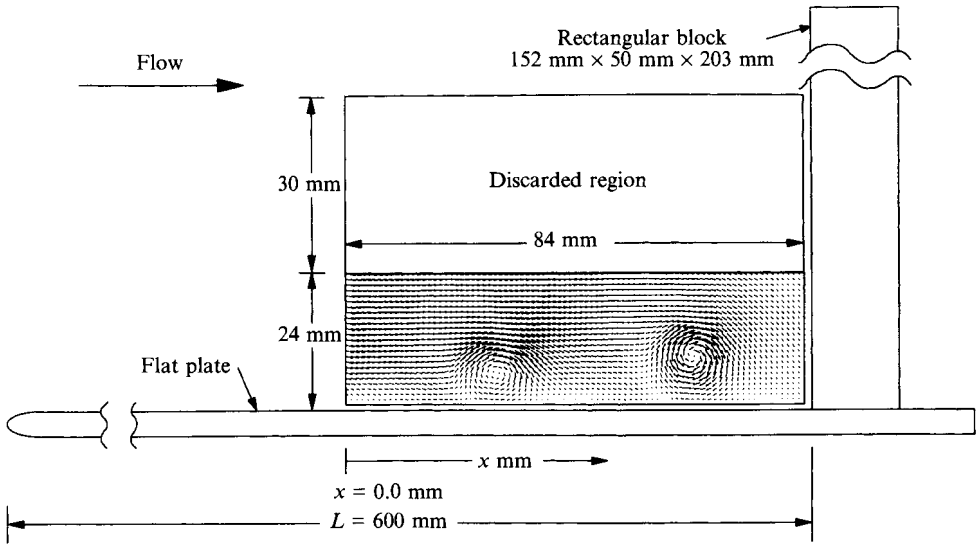

FIGURE 2. Schematic of rectangular block mounting and field of view used for the PIV experiments. $U_\infty = 50.4$ mm s^{-1}, $Re_{\delta^*} = 298$, $Re_L = 3 \times 10^4$.

2. Experimental method

Experiments were performed in a Plexiglas free-surface water channel with a test section 0.3 m deep × 0.9 m wide × 5.0 m long. A rectangular bluff body (20 cm high × 15.2 cm wide × 5.1 cm deep) was mounted on a 2.6 m long (12 mm thick) flat Plexiglas plate with a 5:1 elliptical leading edge. The water depth above the plate was 18.7 cm. The block was located 0.6 m from the leading edge of the plate (figures 1 and 2) and oriented such that the width was perpendicular to the flow direction. The free-stream velocity U_∞ was 50.4 mm s^{-1}, which gave corresponding $Re_L = 3 \times 10^4$ and $Re_{\delta^*} = 298$, based on (i) the distance L from the leading edge to the block, and (ii) the displacement thickness δ^* calculated for an equivalent unobstructed Blasius boundary layer at location L.

Initial flow visualization was performed using a moveable hydrogen-bubble visualization probe consisting of a 25 μm diameter platinum wire soldered taut between two insulated brass rods of a Y-shaped support. The wire is used as the cathode in a process of electrolysis with a variable voltage/frequency power supply providing a pulsed current density to the wire; the anode was a 6.0 mm diameter carbon rod located away from the region of interest. Lighting consisted of either general illumination through the bottom of the channel using a 1050 W photographic lamp, or light sheet illumination created using a 10 W scanned argon-ion laser (Rockwell *et al.* 1993) on the symmetry plane (figures 1 and 3).

High image-density particle image velocimetry (Adrian 1991; Rockwell *et al.* 1993), was used to establish the details of the velocity field. The scanned laser was used to illuminate spherical, metallic-coated particles (nominal diameter of 12 μm and density of 2.6 g cm^{-3}) on the symmetry plane. Approximately 20 cm^3 of particles were mixed in the 2400 gallon water channel, which ensured approximately 15 particle images within each interrogation window (1.7 mm × 1.7 mm in the plane of the laser sheet; see below). The scanned laser sheet was generated using a 72 facet rotating mirror in conjunction with a 10 W Argon-ion laser. An optical assembly employing a convex lens, concave lens, and a singlet lens (Corcoran 1992) was used to focus the beam to a

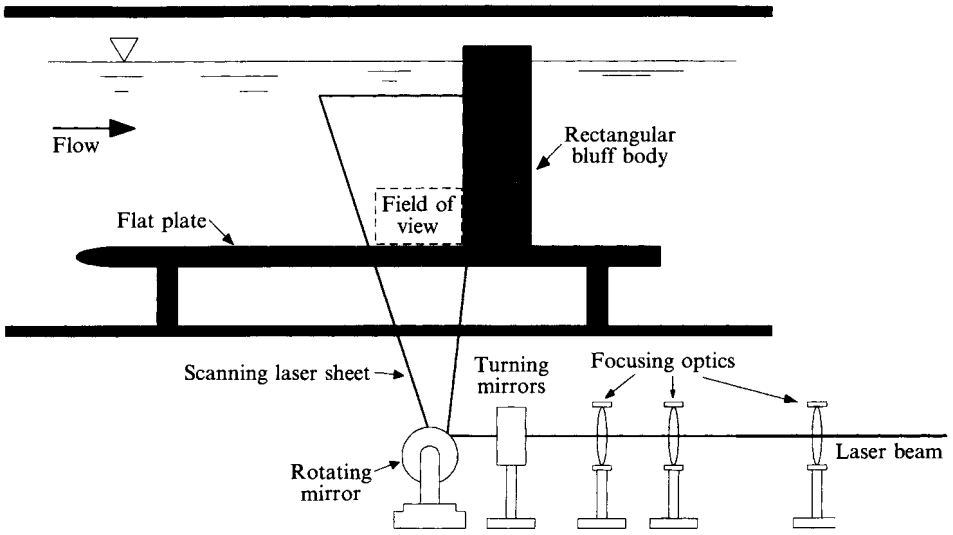

FIGURE 3. Side-view schematic of PIV experimental apparatus, including laser optics.

diameter of approximately 1.0 mm at the region of interest (figures 2 and 3). A combination of a 150 Hz laser scanning rate and a $\frac{1}{30}$ s camera exposure time was employed, which produced image photographs with 5 exposures of each particle within the viewing field. Photographs were taken at a rate of 1 image per second for 10.0 s, capturing a little more than one breakaway cycle. A NIKON F3 35-mm camera (using Kodak TMAX 400 film) was used to record the particle images (figure 4).

A rotating bias mirror, located immediately in front of the camera lens at an angle of 45° to the centreline of the lens (figure 4), imparts a uniform bias velocity to the images of all particles, which overcomes the directional ambiguity associated with regions of reverse (negative) flow (Adrian 1986). The magnitude of the imposed bias was sufficiently large to overcome negative velocities associated with regions of reverse flow, but small enough such that the principal features of the actual velocity field were not obscured. The principal guideline for determining the minimum bias velocity is that a line passing through successive, multiply-exposed particle images should not turn an angle greater than 90° (Towfighi 1992). In order to recover the actual velocity field, the uniform bias velocity is subtracted from the field of vectors obtained from evaluation of the entire image.

In order to evaluate the entire pattern of particle images recorded on 35-mm film, each photographic image is digitized into a TIFF file format, using a Nikon LS-3510AF 35-mm film scanner with a resolution of 125 pixels mm^{-1} of film. The velocity at a given location was evaluated from the digitized image (4125 pixels × 2625 pixels) using a 486 PC with two Eighteen-Eight array processors, employing a single-frame autocorrelation technique involving application of two successive FFTs over an 80 × 80 pixel interrogation window. The interrogation window was moved sequentially across the image in order to establish the velocity at successive locations. In order to approximate the Nyquist sampling criterion, adjacent windows were overlapped by 40%. This evaluation process yielded approximately 4950 velocity vectors per image. Since the magnification M of the camera lens was 1:2.6, the effective width d_I of the interrogation window in the plane of the laser sheet was $d_I/M = 1.7$ mm; correspondingly, the effective grid width was $\Delta l/M = 1.02$ mm in the laser sheet. Owing to a variety of factors, including locally inadequate quality of the principle

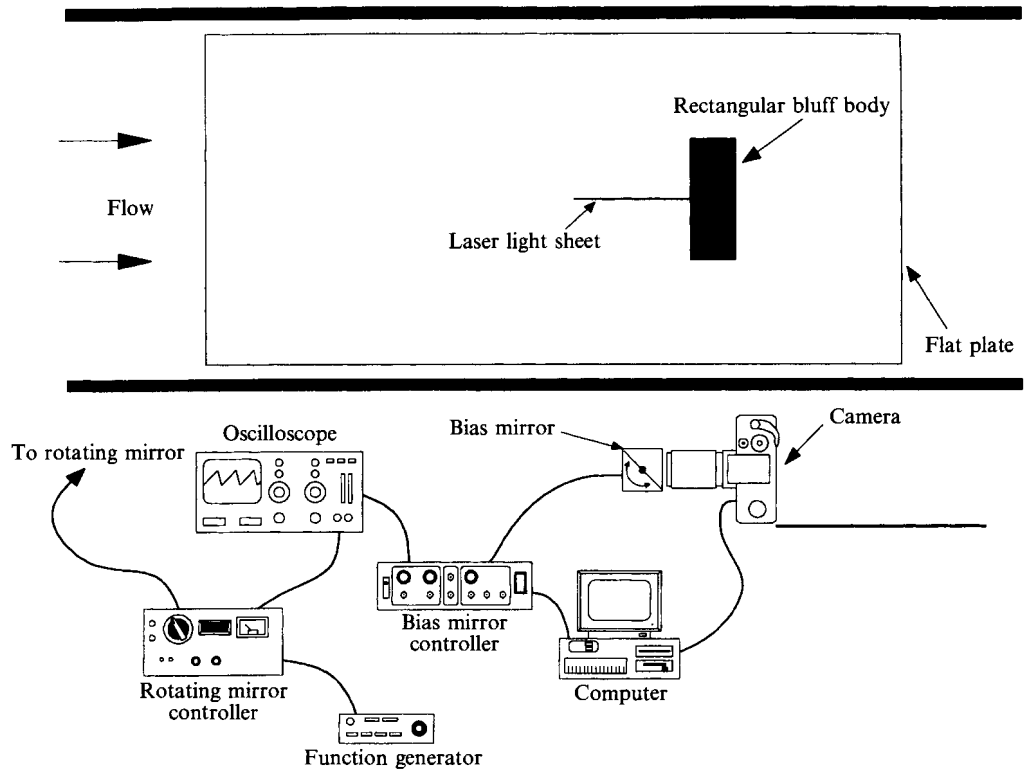

FIGURE 4. Plan-view schematic of PIV experimental apparatus, showing orientation of the bias mirror.

images and insufficient particle concentration, the evaluation process can sometimes yield an incorrect vector or no vector at all. In cases where the vector differed drastically from its neighbours, it was manually deleted. Each of the blank interrogation areas was then replaced by a vector determined by bilinear interpolation. Typically, no more than two to three per cent of the vectors in the entire velocity field had to be established using this interpolation process.

Prior to further processing, the entire field of velocity vectors was smoothed by convolving the field of vectors with a Gaussian kernel having a coefficient $p = 1.3$, which minimizes distortion of the original field of vectors (Landreth & Adrian 1989). No further filtering or smoothing was done in constructing contours of constant vorticity, which were established using a cubic spline fit through the discrete values of vorticity employing a tension factor of 0.1. In certain plots, the levels between vorticity contours were interpolated to emphasize the structural features of the flow. The typical minimum distance between contours was approximately one third of the grid width $\Delta l/M$, with this distance decreasing to as low as one sixth $\Delta l/M$ in a few high-gradient regions. Note that the bottom and right-hand edges of the data field represented solid surfaces; special care was taken to ensure that the no-slip condition was maintained at the bottom surface during post processing.

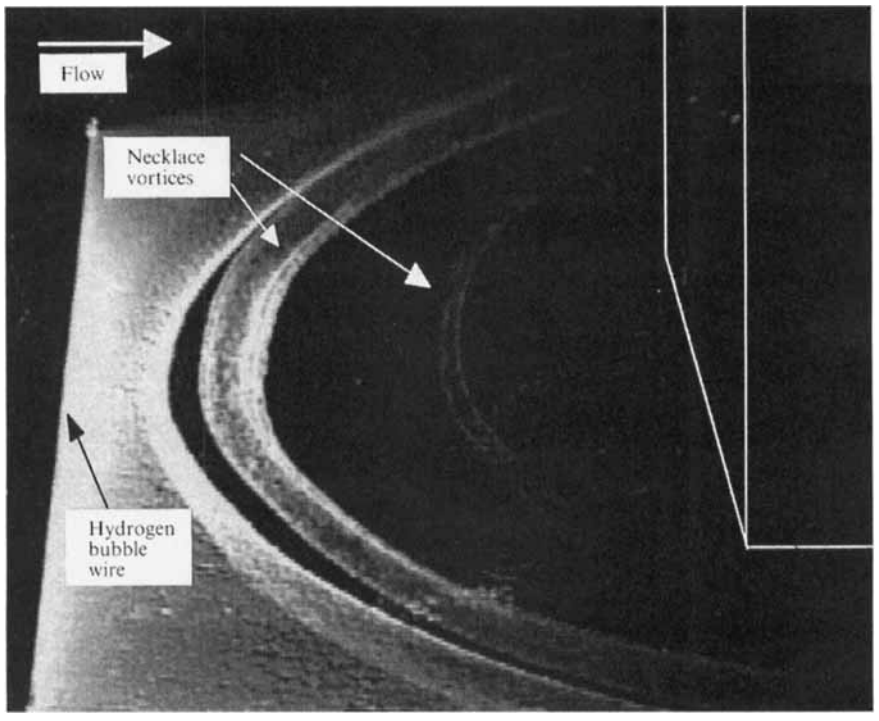

FIGURE 5. Hydrogen-bubble visualization of the necklace vortex system formed at the junction of a rectangular bluff body and flat plate.

3. Results and discussion

3.1. *Flow visualization*

The general characteristics of the breakaway regime examined in this paper were initially established using hydrogen-bubble flow visualization, as illustrated in figure 5. For the flow conditions of this study, the vortex system is unsteady, characterized by the periodic formation of necklace vortices, which subsequently break away and move towards the block; figure 6(*a*) is a cross-sectional hydrogen-bubble visualization with an accompanying schematic illustration (figure 6*b*) of this periodic behaviour as viewed on the symmetry plane. For this particular flow, a primary vortex forms approximately 132 mm upstream of the block ($x = -48$ mm, figure 6(i), (vi); note that a negative x-value specifies a location upstream of the field of view). Following formation, the primary vortex breaks away from the formation region (at approx. $x = -16$ mm) and advects downstream (figure 6(ii)–(vi)). The diameter of the primary vortex just after breakaway is approximately 14–15 mm, which is approximately 81–87% of the equivalent, unobstructed Blasius boundary-layer thickness (δ) at the block location (0.6 m from the leading edge of the plate). As the primary vortex approaches the block, it decelerates and coalesces with a corner vortex in the junction region (figure 6(v)–(vi)). In addition, the vortex is stretched as it advects downstream, reducing the diameter of the vortex to approximately 11–13 mm (64–75% of the equivalent Blasius boundary layer) just prior to amalgamation. Note that the reduction in size of the hydrogen bubble 'ring' marking the necklace vortices (figure 6(*a*)(i)–(vi)) is due to the inward spiralling of the bubbles and is not indicative of the true vortex diameter reduction. The variation in vortex diameter was established using vorticity contours

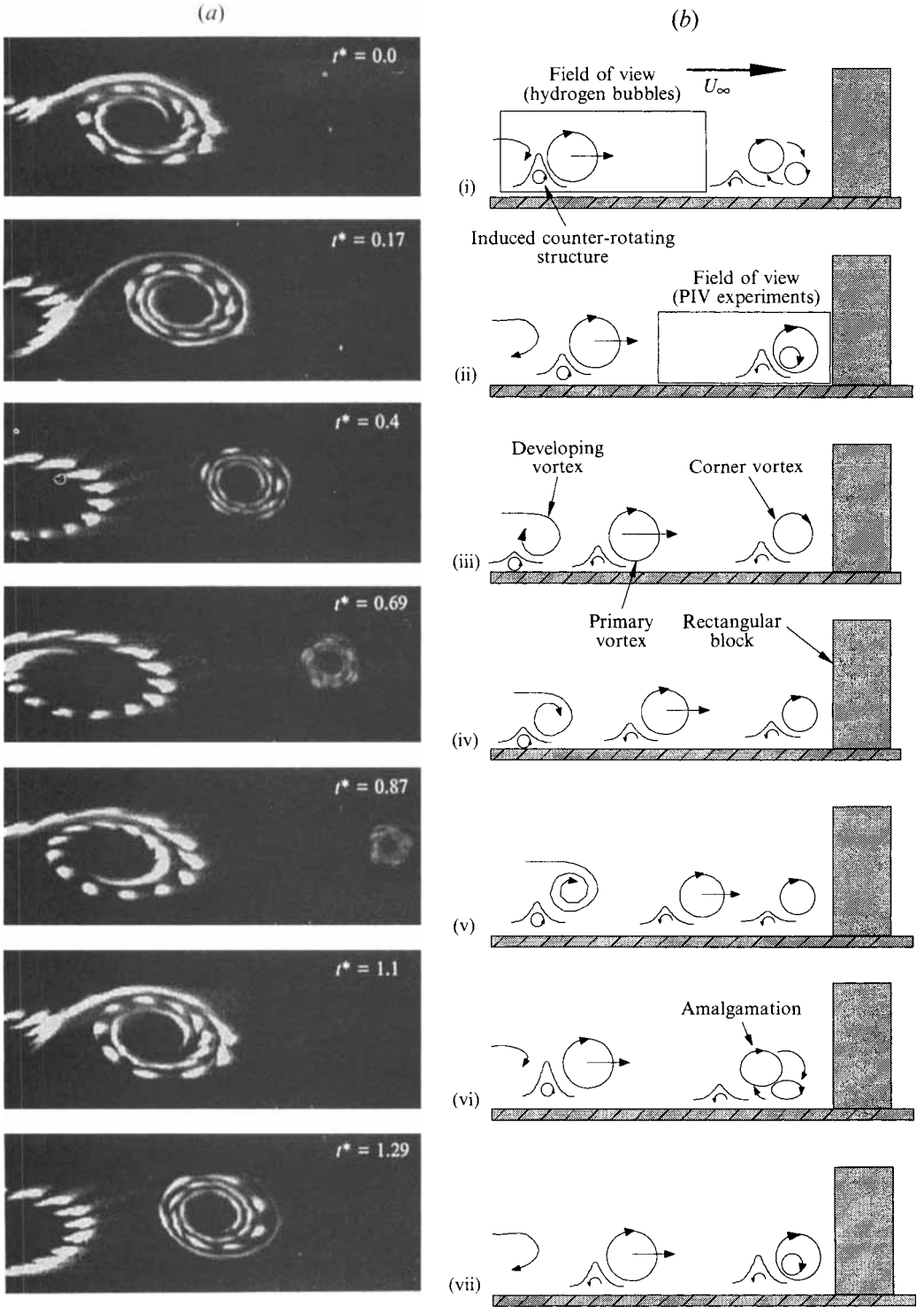

FIGURE 6. Hydrogen bubble visualization (*a*) and corresponding schematic (*b*) (not to scale) time sequence of the breakaway regime, where $t^* = t/T$ (t = time and T is the period of one cycle). The height of the induced counter-rotating structures is an indication of their relative strength.

obtained from the PIV analysis (the criteria is described in §3.5). The new corner vortex formed by the amalgamation remains in the corner region until a new primary vortex arrives and this coalescence process repeats. The corner vortex is also stretched between amalgamations, causing a reduction in its diameter by approximately 25% over a cycle. The repetition frequency of these events was 0.2 Hz, as measured from an extended visualization sequence, giving a Strouhal number based on block width of 0.605 – about 4.65 times higher than the vortex wake shedding Strouhal frequency of 0.13 for a rectangular block of this shape. At any given time during the cycle there are two vortices in different phases of development in the upstream formation region. In addition to the presence of the necklace vortices, eruptions of surface fluid induced by vortex interaction with the surface fluid are also noted, as illustrated in figure 6(*b*). These interaction regions contain vorticity of opposite sign from the necklace vortex, but these regions only infrequently appear as coherent vortices. However, induced counter-rotating vortices are often observed adjacent to the developing vortices in the formation region, as indicated in figure 6 by the small, closed opposite rotation vortex near the surface.

3.2. *Velocity field*

Figure 2 shows an example velocity vector field obtained following post processing of the particle images. The flow field dimensions captured in the PIV experiments were approximately 84 × 54 mm, with the block defining the right edge of the field and the flat plate the bottom of the field of view (figure 2); note that this excludes the formation region (figure 6(*b*)(ii)). This restricted field of view was selected to provide adequate spatial resolution for close examination of the discrete necklace vortex interactions, as well as the smaller-scale structures created near the surface. For the purposes of this paper, the top 30 mm of the field of view, which reflects basically a uniformly decelerating free-stream flow, is not shown (figure 2). The particular velocity field shown in figure 2 reflects quantitatively the phase of the periodic cycle wherein a primary necklace vortex, to the left, is approaching a corner vortex, appearing to the right of the vector field.

The velocity field was used to establish instantaneous streamline patterns, several of which are illustrated in figure 7. Note that the streamline patterns in figures 7(*a*) and 7(*b*) appear markedly different from those described by Baker and others for steady and oscillating vortex systems (e.g. figure 7(*h*) is a steady streamline pattern computed by Visbal 1991). This variance from conventional steady streamline patterns is due to the relatively large vortex advection velocities encountered for the unsteady necklace vortex flow regime examined in this study. As stated by Perry & Chong (1987) in their seminal work on critical point theory, relative motion can have a significant impact on the character of the streamline patterns observed. Comparing the present unsteady streamline patterns (figure 7*a–c*) and the typical steady streamline patterns (e.g. figure 7*h*), the differences are that the steady streamline pattern contains saddle points and foci in the free-slip region, whereas the unsteady patterns display only foci in the free-slip regions, with the saddle points located on the surface in the form of half saddle points. Note that figure 7(*c*), which is near the point of amalgamation with the primary vortex near stagnation, displays a streamline pattern which closely approaches that for the steady prototype. While figures 7(*a*) and 7(*b*) do not conform to the expected steady patterns of figure 7(*h*), they appear qualitatively similar to figure 7(*g*), taken again from the computational results of Visbal (1991) for a junction vortex system in the unsteady regime.

To examine the impact of the relative motion of the vortex flow field on the expected critical point patterns, the flow fields of figures 7(*a*), 7(*b*) and 7(*c*) were transformed

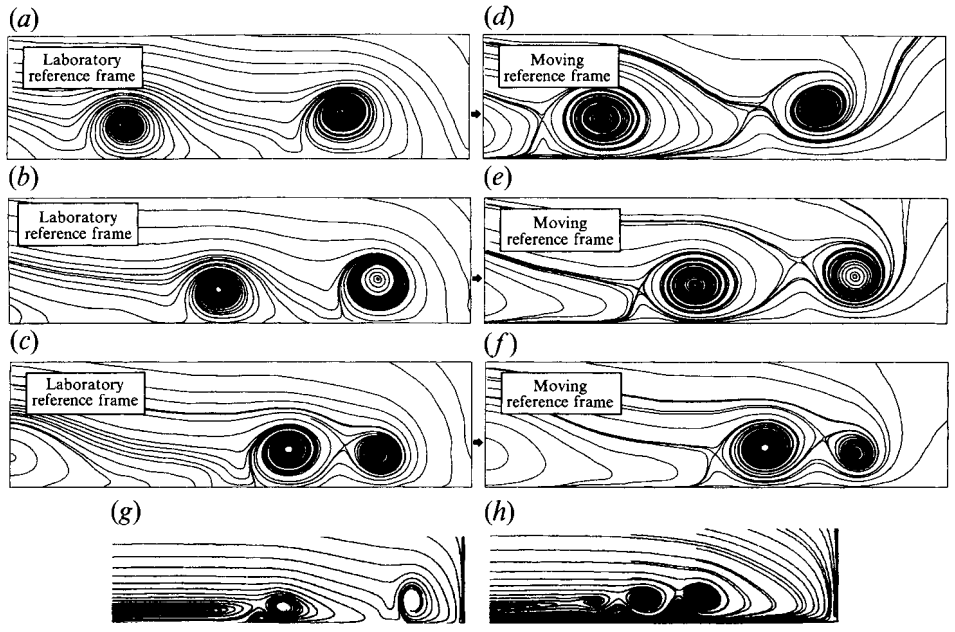

FIGURE 7. Selected streamline patterns. Flow is left-to-right with the body at the right edge of the plots and the flat plate at the bottom. Patterns (*a*), (*b*) and (*c*) are shown in the laboratory reference frame for progressively later instants in a cycle, and correspond to figure 8(*a*)(x), (vi) and (viii), respectively. Patterns (*d*), (*e*) and (*f*) are corresponding patterns to (*a*), (*b*) and (*c*), respectively, as viewed from a transformed reference frame moving with the primary vortex (on the left), with pattern (*d*) of the attachment type, and patterns in (*e*) and (*f*) reflecting a jet maze topology. Patterns (*g*) and (*h*) are computed results from Visbal (1991) for a cylinder–flat plate junction in air for unsteady ($Re_D = 5400$, $\delta_0/D = 0.1$) and steady ($Re_D = 2600$, $\delta_0/D = 0.1$) cases, respectively.

from a laboratory frame to a reference frame advecting with the primary vortex in each field; the subsequent streamline patterns appear respectively as figures 7(*d*), 7(*e*) and 7(*f*). Note that these transformed streamline patterns more closely emulate the standard steady necklace vortex topology shown by Visbal (figure 7*h*) and initially described by Baker (1979). Note however, that while figure 7(*d*) (early in the cycle) reflects a streamline topology essentially identical to the steady attachment topology described by Visbal (1991), figures 7(*e*) and 7(*f*) (later in the cycle) exhibit a pattern characteristic of what is termed jet maze topology. The significance of this change in character is not immediately clear, but suggests a possible change in the mechanisms involved in the flow throughout a cycle, possibly due to the transient behaviour of this flow regime. It was expected that the choice of the transformation velocity for the moving reference frame would be of critical importance (Perry & Chong 1987) since streamlines are velocity dependent. For the present study, the transformation velocity (the advection velocity of the vortices) was determined as the average advection velocity of the primary vortex inferred between two successive data sets taken one second apart. Since the primary vortex is decelerating as it approaches the block, this average advection velocity is at best a close approximation to the true advection velocity. However, an examination of the influence of the transformation velocity on the resultant streamline patterns revealed that variations of the transformation velocity are not critical, since a shift in the transformation velocity by as much as $\pm 30\,\%$ would shift the location of the critical points in the flow, but the general character of the streamline pattern would be preserved.

An additional observation from the streamline patterns is the presence of what appear to be limit cycles (Perry & Steiner 1987) within the vortices, wherein the streamlines spiral into circular limiting streamlines of constant radius. This characteristic appears to varying degrees throughout figure 7; for example, figure 7(*c*) illustrates both a stable limit cycle (i.e. a slow spiralling inward of external streamlines to a fixed radius limiting streamline in the vortex, and a slow outward spiralling of streamlines from the vortex centre to the limiting streamline) in the primary vortex, and a series of closed streamlines inside the corner vortex. When limit cycle behaviour was not observed in the flow field results (approximately 50% of the time), the streamlines spiralled slowly into the centre of the vortex, in a manner consistent with the streamline results of Visbal (1991). Note that this limit cycle behaviour and slow inward spiralling of the streamlines are consistent with a flow field that is nearly two-dimensional, and suggests that although the necklace vortices undergo some stretching as they advect inward toward the bluff body juncture, stretching plays only a minor role in the dynamics of the flow field on the symmetry plane.

3.3. *Vorticity field*

Since numerical derivative computations are subject to high uncertainties, a Stokes' theorem approach was used in lieu of a finite-difference representation of the defining equation

$$\omega_z = \frac{\partial v}{\partial x} - \frac{\partial u}{\partial y}, \tag{1}$$

to reduce the uncertainty of the vorticity calculations. Thus, the z-direction vorticity field was established using Stokes' theorem, which can be written generally as:

$$\iint_A \boldsymbol{\omega} \cdot \mathrm{d}\boldsymbol{A} = \oint_c \boldsymbol{u} \cdot \mathrm{d}\boldsymbol{s}. \tag{2}$$

Assuming the vorticity to be constant over $\boldsymbol{A}$, the z-direction vorticity is given by

$$\omega_z = \frac{1}{4\delta_x \delta_y} \oint_c \boldsymbol{u} \cdot \mathrm{d}\boldsymbol{s}, \tag{3}$$

where δ_x and δ_y are the step sizes between two adjacent velocity vectors in the x- and y-directions, respectively. The vorticity at a point was calculated from equation (3) by numerically integrating around a rectangular path defined by the eight points adjacent to a selected point.

Figure 8(*a*) is a time sequence of the measured vorticity fields covering 10 s of the flow (about 2 cycles). In this figure, clockwise rotation corresponds to negative vorticity and is indicated by dashed lines; conversely, positive vorticity is indicated by solid lines. The iso-vorticity levels range from $\pm 1 \rightarrow \pm 41\ \mathrm{s}^{-1}$ in intervals of $4\ \mathrm{s}^{-1}$. The sequence show in figure 8(*a*) provides a detailed illustration of the vorticity characteristics of the breakaway necklace vortex system in proximity to the rectangular body. As the sequence begins (figure 8(*a*)(i)), a primary vortex has just begun to amalgamate with the corner vortex. As time progresses, a new primary vortex, formed out of the field of view, is advected downstream, entering at the left of the field of view (figure 8(*a*)(iii)) with an advection velocity of approximately 36% of the local free-stream velocity ($u_{adv}/U_{\infty,local}$); note that $U_{\infty,local}$ is defined as the velocity well outside the boundary layer at the same streamwise distance from the block as the advecting vortex. The primary vortex decelerates as it approaches the block, with ($u_{adv}/U_{\infty,local}$)

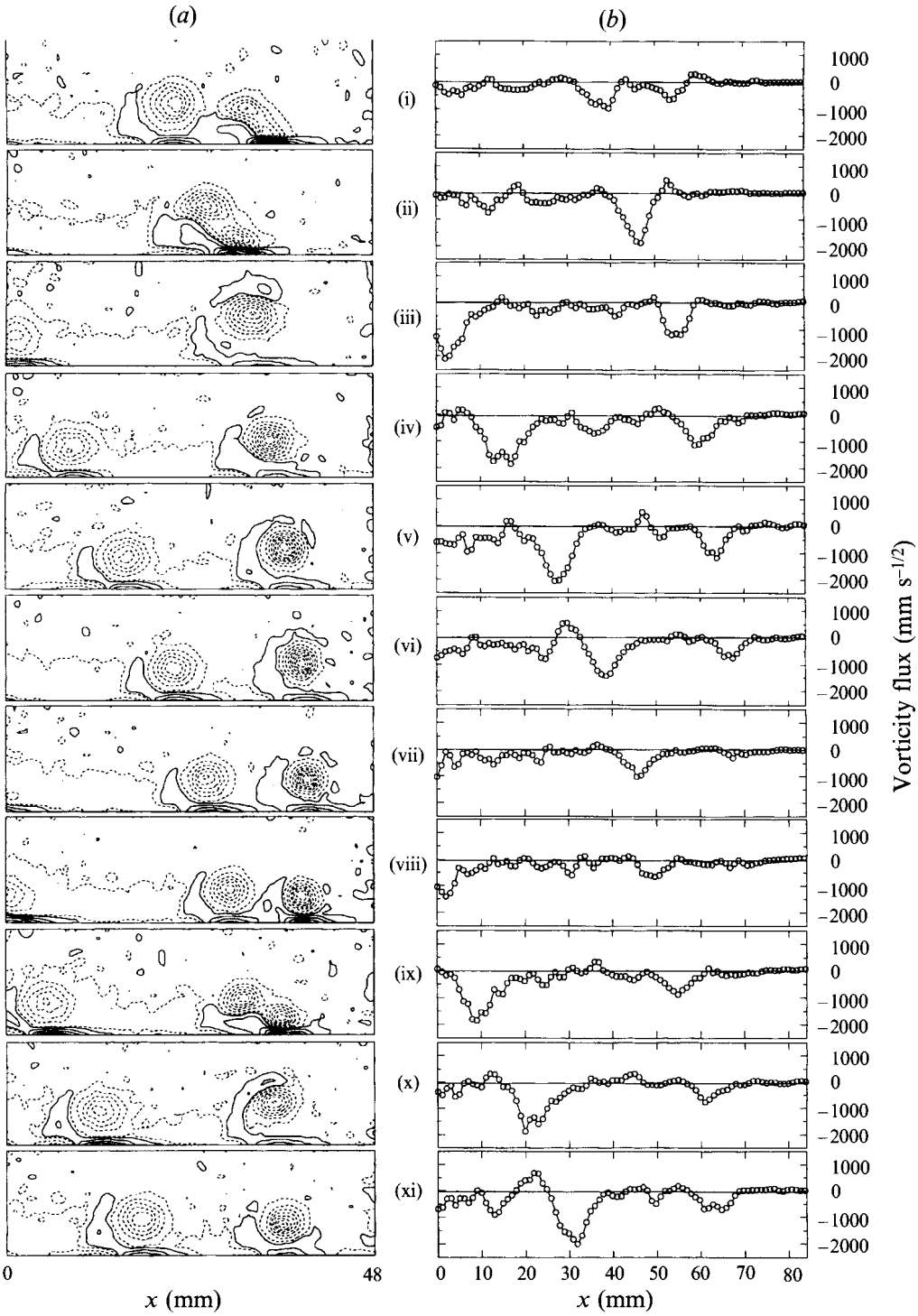

FIGURE 8. (*a*) Vorticity contours. Dashed lines indicate negative vorticity, solid lines indicate positive vorticity. Time between frames is 1.0 s. (*b*) Vorticity flux.

remaining roughly constant until just prior to amalgamation, when the advection velocity drops to approximately 28% of the local free-stream velocity, and amalgamation with the corner vortex begins (figure 8(*a*)(ix)).

Also apparent from figure 8(*a*) is the development of concentrated opposite-sign vorticity generated near the trailing portion of the necklace vortices, which is the result of the interaction of the local vortex-generated pressure gradient with the surface fluid. This localized opposite-sign vorticity concentrates, lifts from the surface, and ejects into the outer field, at times circumventing the original vortex, and apparently cross-cancelling with the vorticity of the generating vortex (see §3.5 below). Note that Visbal (1991), in his computational study of the laminar necklace vortex system formed at a cylinder–flat plate juncture, also noted the aforementioned eruptions of opposite-sign vorticity caused by the interaction of the necklace vortices with a surface. Additionally, similar localized vortex-induced eruptive behaviour has been observed previously in studies by Harvey & Perry (1971) of trailing vortices adjacent to the ground, Peace & Riley (1983) of a vortex pair in ground effect, Walker *et al.* (1987) of a ring vortex interaction with a surface, and Robinson (1991) in a detailed assessment of wall-region vortex interactions for a computationally simulated turbulent boundary layer. However, a unique aspect of the present study is the clear quantitative illustration of how these localized, vortex-indued regions of discrete vorticity of opposite sign evolve and engirdle the generating vortex, and (as is illustrated in §3.5) undergo a process of vorticity cross-cancellation which continuously 'nibbles' away and weakens the discrete vorticity concentration within the necklace vortices.

The mechanism for this eruptive behaviour has been clearly illustrated by Peridier, Smith & Walker (1991) in a computational study of the unsteady boundary-layer separation induced by the pressure gradient field due to a two-dimensional vortex in motion above an infinite plate. Peridier observed the development of focused eruptions of boundary-layer fluid near the trailing edge of the vortex caused by the interaction of the vortex with the surface. While Peridier's study examined the problem in the limit $Re \rightarrow \infty$ (much higher than the present study), the character of the behaviour observed in the present necklace vortex system is essentially the same as that described by Peridier, suggesting that the mechanisms for the generation of these eruptions (i.e. local vortex-imposed pressure gradients) are the same.

3.4. *Vorticity flux*

Figure 8(*b*) is a series of vorticity flux plots which correspond to the vorticity plots of figure 8(*a*). Vorticity flux (Φ_ω) is computed using the expression

$$\Phi_\omega = \int_0^h \omega u \, \mathrm{d}y, \tag{4}$$

which reflects the streamwise flux of vorticity across a vertical cross-section of the flow field. The vorticity flux provides a measure of the instantaneous vorticity transport at any streamwise location at a particular time. The peaks of vorticity flux which appear in figure 8(*b*) generally correspond to the necklace vortex position (negative peaks) or the surface generated vorticity (positive peaks). Note that from figure 8(*b*)(iii) to 8(*b*)(ix) the vorticity flux associated with the primary vortex appears to systematically decrease as the vortex advects downstream, which suggests a 'loss' of vortex strength as the vortices approach the block, prior to amalgamation with the corner vortex.

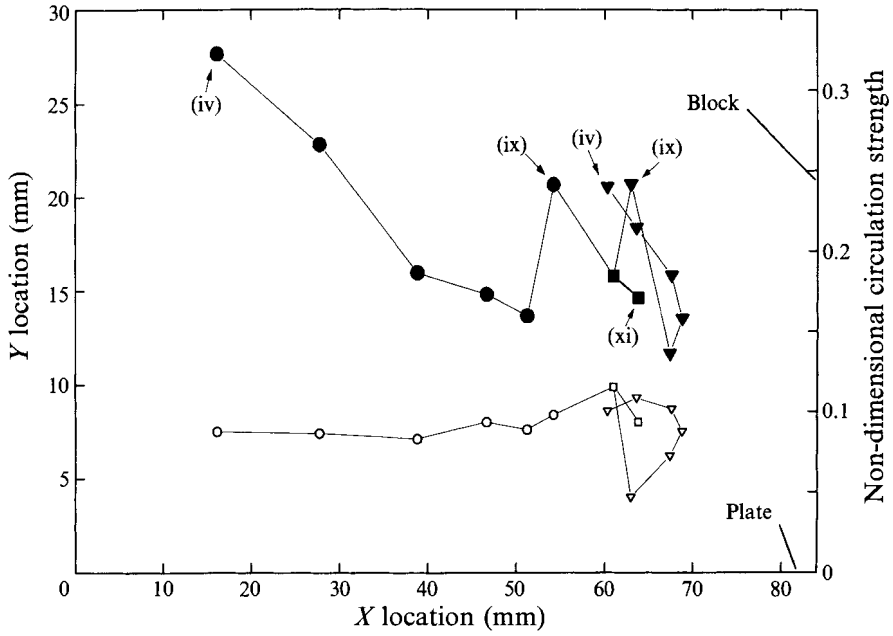

FIGURE 9. Vortex trajectory (open symbols) and non-dimensional strength (Γ_v/Γ_e, closed symbols), where Γ_e is the time integral of vorticity flux passing across the left edge of the field of view over one cycle. Plotted data corresponds to figures 8(iv)–8(xi). ○, impinging primary vortex; △, corner vortex; □, new corner vortex after amalgamation.

3.5. *Circulation and trajectory*

The circulation of individual vortices was calculated from the velocity field using the line integral

$$\Gamma_v = \oint V \cdot \mathrm{d}s, \tag{5}$$

and integrating numerically around a contour of minimal constant vorticity (where $\omega = -1.0\ \mathrm{s}^{-1}$ was taken as the essential boundary of a vortex). Figure 9 is a plot of non-dimensional vortex strength (Γ_v/Γ_e, closed symbols) and vortex trajectory (open symbols), corresponding to the sequence figure 8(iv)–8(xi). The vortex strength is non-dimensionalized on an equivalent cyclic circulation term (Γ_e) obtained by integrating the vorticity flux passing through the left-hand side of the field of view over approximately one cycle (figure 8(iii)–8(x)); this gave a cycle strength of approximately $-4500\ \mathrm{mm}^2\ \mathrm{s}^{-1}$, and represents the equivalent circulation strength of the vorticity advected into the field of view over one cycle. The circles in figure 9 indicate the centre of the incoming primary vortex, the triangles show the centre of the initial corner vortex, and the squares show the centre of the new corner vortex following amalgamation. Note that the primary vortex enters from the left and follows an essentially level path as it is advected downstream, while the corner vortex moves in a roughly circular path; at the point of amalgamation, the corner vortex is pulled beneath the primary vortex. Notice that each vortex continuously decreases in strength up to the point of amalgamation. The primary vortex enters the field of view at a circulation strength of approximately 33% of the equivalent cyclic circulation strength, decreasing to approximately 15% just before amalgamation. The corner vortex exhibits similar behaviour, with an initial strength of about 25%, and decreasing to approximately 13% before amalgamation. During amalgamation, the new corner

vortex increases sharply in strength, from about 13% to 25%, owing to the additional vorticity contributed by the primary vortex. However, immediately following amalgamation, the new corner vortex experiences a sharp decrease in strength. Note that the points on figure 9 which correspond to the amalgamating vortices of figure 8(*a*)(ix) are indicated by different positions, but reflect the same strength for each vortex; this is because figure 8(*a*)(ix) is at the initiation of the amalgamation process, and the $\omega = -1\ s^{-1}$ contour (used to define the vortex strength, as mentioned above) engirdles both vortices, such that the strength of both vortices is merged, although the locations are still distinct. It is hypothesized that cross-cancellation of vorticity between the necklace vortices and the ejected opposite-sign vorticity is the major mechanism causing the observed decrease in strength of both the primary and corner vortices.

Because the necklace vortices deform three-dimensionally as they approach the block, they undergo a process of stretching by the flow around the ends of the block. It is well known that during stretching of an isolated vortex the circulation will remain conserved in the absence of flux or diffusion across a boundary which initially encompasses all the vorticity. Since the present measurements indicate that the necklace vortex strength (as measured about the minimum vorticity contour) continually diminishes, this suggests that viscous effects must be responsible for the decrease. There are basically two ways that viscous effects could manifest themselves. First, vorticity could diffuse across the $\omega = -1\ s^{-1}$ contour used to establish the vortex strength; secondly, the vorticity cross-cancellation could occur between the necklace vortex and its corresponding surface-generated vorticity.

To examine the possible effects of viscous diffusion, the cross-section of a necklace vortex was modelled as a decaying Oseen vortex in a quiescent medium. Typical velocity profiles measured across a necklace vortex (see figure 11) were used to model a comparable strength and diameter (at $\omega = -1\ s^{-1}$) Oseen vortex in an equivalent state of decay. The change in circulation of the Oseen vortex from this initial condition over a four second period (the period of measured vortex decay from figure 8(*a*)(iv) to 8(*a*)(vii)) was determined using $\omega = -1\ s^{-1}$ as the boundary for the circulation strength. This indicated a potential decrease of circulation strength of the Oseen vortex of about 8.0% owing to diffusion of vorticity across the $\omega = -1\ s^{-1}$ boundary. However, figure 9 indicates a decrease of approximately 50% for the same four second period from figure 8(*a*)(iv) to 8(*a*)(vii) (i.e. from the time the primary vortex enters the field of view until just prior to amalgamation). This model suggests that diffusion can play only a small part in the decrease of inferred vortex strength, and that vorticity cross-cancellation is the probable mechanism for the observed vortex decay. Re-examining figure 8(*a*) clearly shows this process in action, as the tongues of positive vorticity are observed to project away from the surface and engirdle the necklace vortices. Clearly, a continuous process of generation and ejection of opposite-sign vorticity, followed by engirdlement and cross-cancellation with the initiating vortex is the key mechanism in the observed rapid decrease in vortex strength and in establishing a balance of the vorticity field within the junction region.

3.6. *Velocity profiles*

The velocity field data were also used to examine selected u-velocity profiles, both for assessment of how the boundary layer is modified by the presence of the necklace vortex system and to examine the velocity distribution in the core of the necklace vortices. Figures 10(*a*) and 10(*b*) show selected velocity profiles for two frames of data (figure 8(*a*)(v) and 8(*a*)(ix)). These suggest that the velocity distribution within the

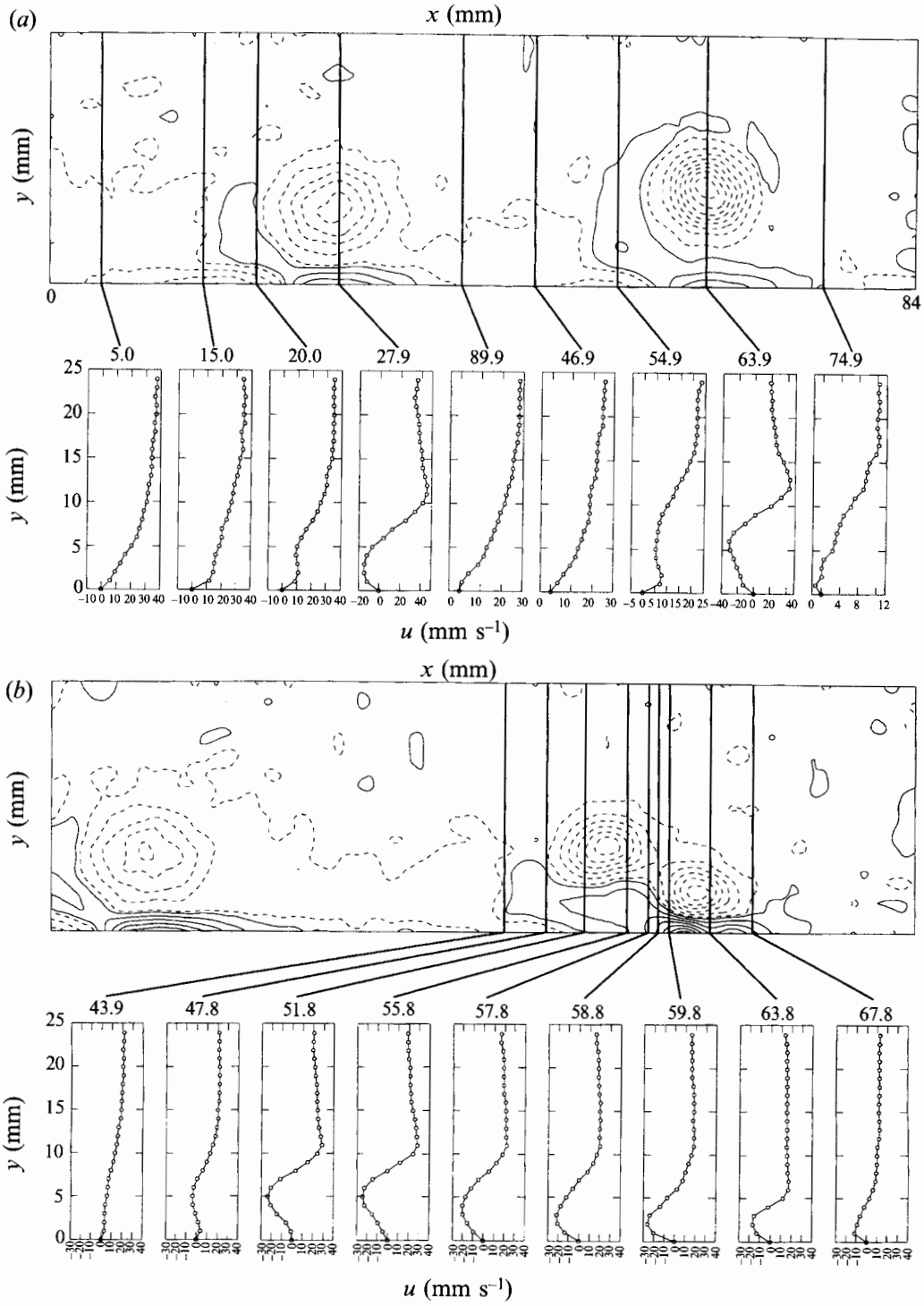

FIGURE 10. (*a*) Selected *u*-velocity profiles for figure 8(*a*)(v). (*b*) Selected *u*-velocity profiles for figure 8(*a*)(ix).

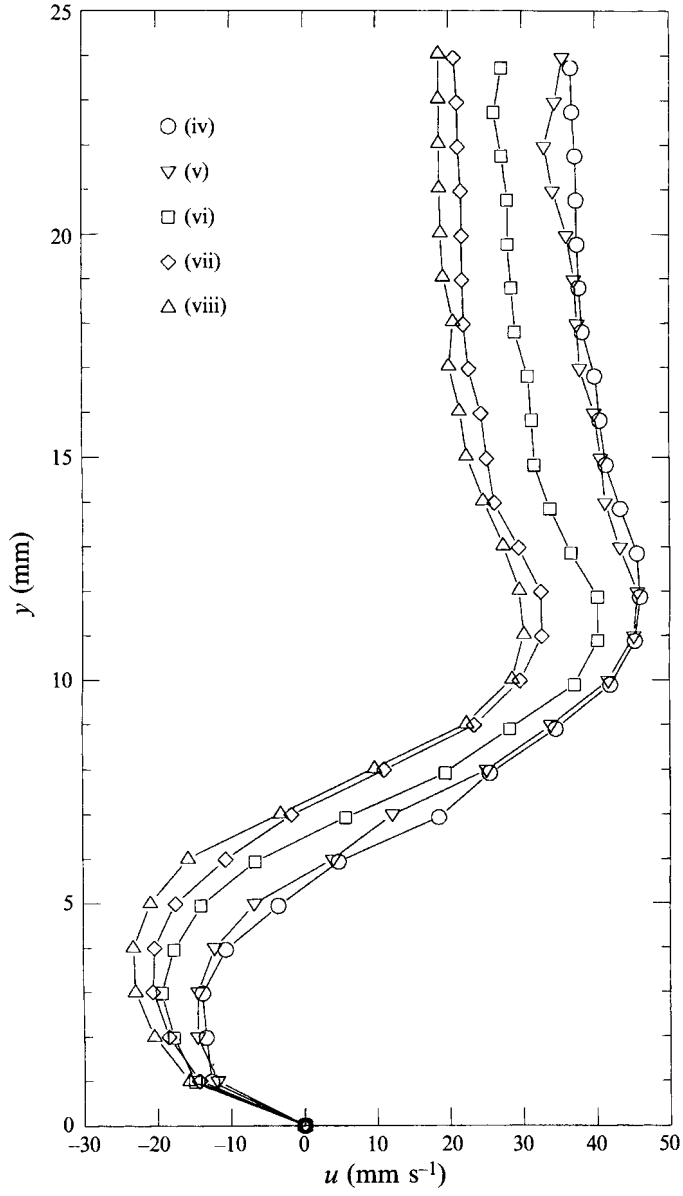

FIGURE 11. Centreline velocity profiles of a necklace vortex convecting downstream. Profiles correspond to the centreline of the primary vortex shown in figures 8(*a*)(iv) to 8(*a*)(vii). Each profile is taken at one second intervals.

vortex core is quite similar to that of a combined Rankine vortex, with a central core which is strongly similar to solid-body rotation. Figure 10(*a*) also illustrates that the profile shape is rather Blasius-like between vortices, taking on inflexional characteristics within the regions of surface-generated, positive vorticity. Note that the general behaviour of these collective profiles in the vicinity of the primary vortex appears to be coincident with similar profiles determined by Visbal (private communication) from his previously published computational study of unsteady cylinder juncture flows (Visbal 1991), including the combined Rankine behaviour of the vortex core, and the inflexional behaviour in the induced vorticity regions.

Note that inflexional profile behaviour, similar to that shown in the induced vorticity regions of the present study, has also been shown computationally (Peridier *et al.* 1991) to be indicative of vortex-induced boundary-layer separation in the limit $Re \to \infty$. Peridier showed that pronounced inflexional velocity profiles were manifested in the eruptive regions induced by a vortex above an infinite plate. The inflexional profiles observed in the present study are less pronounced because the necklace vortices were much weaker than those studied by Peridier. However, the similar profile behaviour suggests that the eruptive mechanisms observed in this study are probably the same as those revealed by Peridier.

Figure 11 shows the collective centreline velocity profiles for the advecting primary necklace vortex (shown in figures 8(*a*)(iv)–8(*a*)(vii)). In this figure, the similarity of the core profile to that of a combined Rankine vortex is quite marked, with the profiles remaining relatively invariant as the vortex advects toward the block.

4. Conclusions

The laminar necklace vortex system formed at a rectangular body–flat plate junction was examined qualitatively and quantitatively to establish the dynamics of the necklace vortex system, the distribution of system vorticity, and the process of vorticity balance within the system. Analysis of visualization and PIV results indicate that:

1. For the flow conditions examined, the necklace vortex system is unsteady, characterized by the periodic formation and subsequent breakaway of necklace vortices upstream of the block; the vortices advect downstream towards the block, at a diminishing fraction of the local free-stream velocity, and undergo an amalgamation process with a corner vortex.

2. The streamline patterns for the unsteady necklace vortex system differ from conventional steady flow patterns in the laboratory frame, requiring transformation to an advected reference frame moving with the primary vortex to reveal consistency of the streamline patterns with steady flow patterns.

3. The advecting, primary necklace vortices exhibit velocity profile behaviour similar to that of an advecting combined Rankine vortex.

4. The necklace vortices interact with surface fluid adjacent to the plate, generating concentrated regions of opposite-sign vorticity, which eject from the surface, at times engirdling the necklace vortex.

5. The necklace vortices undergo a systematic decrease in circulation strength owing to the cross-cancellation of the vorticity comprising the necklace vortices with induced opposite-sign vorticity generated by interaction of the necklace vortices with surface fluid.

The authors wish to thank Dr J. D. A. Walker, Mr J. P. Fitzgerald, and Dr M. Visbal for advice and assistance. We also wish to thank the Air Force Office of Scientific Research for its support of this research under contract no. AFOSR-91-0218. The continuing support of the AFOSR is gratefully acknowledged.

REFERENCES

ADRIAN, R. J. 1986 Image shifting technique to resolve directional ambiguity in double-pulsed velocimetry. *Appl. Opt.* **25**, 3855–3858.

ADRIAN, R. J. 1991 Particle-imaging techniques for experimental fluid mechanics. *Ann. Rev. Fluid Mech.* **23**, 261–304.

BAKER, C. J. 1979 The laminar horseshoe vortex. *J. Fluid Mech.* **95** (2), 347–367.

BLEVINS, R. D. 1990 *Flow-Induced Vibrations*, 2nd edn., Van Nostrand Reinhold.

CORCORAN, T. E. 1992 Control of the wake from a simulated blade by trailing-edge blowing. MS thesis, Department of Mechanical Engineering and Mechanics, Lehigh University.

GRECO, J. J. 1990 The flow structure in the vicinity of a cylinder-flat plate junction: flow regimes, periodicity, and vortex interactions. MS thesis, Department of Mechnical Engineering and Mechanics, Lehigh University.

HARVEY, J. K. & PERRY, F. J. 1971 Flow field produced by trailing vortices in the vicinity of the ground. *AIAA J.* **9**, 1659–1660.

LANDRETH, C. C. & ADRIAN, R. 1989 Measurement and refinement of velocity data using high-image-density analysis in particle image velocimetry. *Applications of Laser Anemometry to Fluid Mechanics* (ed. R. J. Adrian, T. Asauuma, D. F. G. Durão, F. Durst & J. H. Whitelaw). Springer.

LUGT, H. J. 1983 *Vortex Flow in Nature and Technology*. John Wiley & Sons.

MASON, P. J. & MORTON, B. R. 1987 Trailing vortices in the wakes of surface-mounted obstacles. *J. Fluid Mech.* **175**, 247–293.

NORMAN, R. S. 1972 On obstacle generated secondary flows in laminar boundary layers and transition to turbulence. PhD dissertation, Department of Mechanics/Mechanical and Aerospace Engineering, Illinois Institute of Technology.

PEACE, A. J. & RILEY, N. 1983 A viscous vortex pair in ground effect. *J. Fluid Mech.* **129**, 409–426.

PERIDIER, V. J., SMITH, F. T. & WALKER, J. D. A. 1991 Vortex-induced boundary-layer separation. Part 1. The unsteady limit problem $Re \rightarrow \infty$. *J. Fluid Mech.* **232**, 99–131.

PERRY, A. E. & CHONG, M. S. 1987 A description of eddying motions and flow patterns using critical-point concepts. *Ann. Rev. Fluid Mech.* **19**, 125–155.

PERRY, A. E. & STEINER, T. R. 1987 Large-scale vortex structures in turbulent wakes behind bluff bodies. Part 1. Vortex formation processes. *J. Fluid Mech.* **174**, 233–270.

ROBINSON, S. K. 1991 Coherent motions in the turbulent boundary layer. *Ann. Rev. Fluid Mech.* **23**, 601–639.

ROCKWELL, D., MAGNESS, C., TOWFIGHI, J., AKIN, O. & CORCORAN, T. 1993 High image-density particle image velocimetry using laser scanning techniques. *Exps Fluids* **14**, 181–192.

SCHWIND, R. G. 1962 The three-dimensional boundary layer near a strut. *Gas Turbine Lab. Rep.* 67, MIT.

THOMAS, A. S. W. 1987 The unsteady characteristics of laminar juncture flow. *Phys. Fluids* **30**, 283–285.

TOWFIGHI, J. 1992 Instantaneous structure of vortex breakdown on a delta wing. MS thesis, Lehigh University.

VISBAL, M. R. 1991 The laminar horseshoe vortex system formed at a cylinder/plate juncture. *AIAA 22nd Fluid Dyn., Plasma Dyn. & Lasers Conf.* AIAA 91-1826.

WALKER, J. D. A., SMITH, C. R., CERRA, A. W. & DOLIGALSKI, T. L. 1987 The impact of a vortex ring on a wall. *J. Fluid Mech.* **181**, 99–140.